Check for updates

Synthesis of pearl necklace-like ZnO–ZnWO$_4$ heterojunctions with enhanced photocatalytic degradation of Rhodamine B

Yanyan Hao,†[a] Liyun Zhang,†[b] Ying Zhang,*[a] Lin Zhao[a] and Bingsen Zhang [ID] *[b]

Pearl necklace-like ZnO–ZnWO$_4$ heterojunctions composites have been designed and synthesized. The photocatalytic activity of the ZnO–ZnWO$_4$ heterojunctions depended on the calcination temperature and ZnO–ZnWO$_4$ molar ratio. The ZnO–ZnWO$_4$ composites showed higher degradation efficiency than that of ZnO or ZnWO$_4$ individually. The photocatalytic reaction was enhanced due to the heterojunctions construction, which improved charge separation of the photogenerated electron–hole pairs.

1 Introduction

Using semiconductor photocatalysts to solve environmental remediation, especially waste water decontamination, has attracted extensive attention.[1] Zinc oxide (ZnO) plays an important role in degrading various organic pollutants due to its high activity, low cost, and environmental friendliness.[2] In the past decade, various morphological ZnO, such as rods, sheets, flowers, hollow nanostructures, porous structures, and core–shell structures, have been synthesized by hydrothermal, electrospinning, and sol–gel methods.[2,3] Despite achieving great success in the controlled synthesis of single-component ZnO, the photocatalytic efficiency still needs to be improved because of the rapid recombination reaction of photogenerated charge carriers for single semiconductor. Recently, heterostructure composite materials have attracted much attention, because it can improve the primary properties of the constituent materials and create novel functions. Some heterostructure composites have been developed by coupling ZnO with other semiconductors, such as ZnO–WO$_3$,[1b,4] ZnO–CdS,[5] ZnO–TiO$_2$,[6] ZnO–BiVO$_4$,[7] and ZnO–SnO$_2$.[8] Only few works, however, focused on the synthesis of ZnO–ZnWO$_4$ heterojunctions as well as their employment for the photodegradation of organic compounds.[9]

Zinc tungstate (ZnWO$_4$) has received considerable attention as an ultraviolet (UV) light driven photocatalyst due to its relatively high activity for degradation of organic compounds.[10] Amouzegar *et al.* reported cubic-shaped nanocrystalline ZnWO$_4$

prepared by microwave-assisted precipitation technique showed high photocatalytic activity for the degradation of aqueous solution of Rhodamine B (RhB).[11] ZnWO$_4$ was also efficient for the decomposition of malachite green,[12] 4-chlorophenol,[13] and methyl orange.[14] Herein, ZnO–ZnWO$_4$ heterostructure with pearl necklace-like morphology was prepared by precipitation method followed by calcination process. Compared with single ZnO and ZnWO$_4$ phase, the as-obtained ZnO–ZnWO$_4$ heterostructure shows an enhanced photocatalytic activity in the photodegradation of RhB.

2 Experimental

2.1 Sample synthesis

For preparing the Zn(OH)$_2$ precursor, NH$_4$OH solution (25%) was slowly dropped into the vigorously stirred Zn(CH$_3$COO)$_2$·2H$_2$O solution with 0.06 mol L^{-1} concentration until the pH value reached 10.6. The mixed solution was then heated at 80 °C for 2 h to produce Zn(OH)$_2$ precipitate. The precipitate was collected by pump filter and rinsed three times with deionized water and ethanol, respectively. Subsequently, the washed precipitate was dried at 80 °C overnight. For preparing tungstic acid (H$_2$WO$_4$) precursor, 15 g ammonium tungstate was dissolved in 150 mL deionized water under vigorous stirring for 30 min. Following, 30 mL nitric acid (3 mol L^{-1}) solution was slowly added into the above solution and the mixed solution was further stirred for 1 h at 80 °C. The precipitate produced was collected and washed three times with deionized water and ethanol, respectively. The washed sediment was dried at 80 °C overnight to form the H$_2$WO$_4$ precursor.

In order to obtain powders with ZnO/ZnWO$_4$ molar ratios equalling to 1/0.04, 1/0.08, 1/0.12, the amounts of the precursors were opportunely determined. The corresponding samples were denoted as Z-ZW$_{0.04}$, Z-ZW$_{0.08}$ and Z-ZW$_{0.12}$, respectively. A certain amount of Zn(OH)$_2$ and H$_2$WO$_4$ with an equal number

[a]College of Chemistry, Chemical Engineering and Environmental Engineering, Liaoning Shihua University, West No 1 Dandong Road, Wanghua District, Fushun 113001, China. E-mail: zhangying@lnpu.edu.cn

[b]Shenyang National Laboratory for Materials Science, Institute of Metal Research, Chinese Academy of Sciences, 72 Wenhua Road, Shenyang 110016, China. E-mail: bszhang@imr.ac.cn

† The authors contribute equally to this paper.

of Zn and W atoms were used to prepare pure $ZnWO_4$. Pure ZnO was synthesized only using $Zn(OH)_2$ as precursor. Finally, the photocatalysts were obtained by calcining the precursors for 2 h at different temperatures.

2.2 Characterization techniques

The phase composition and crystallinity of the prepared samples were analysed by X-ray diffraction (XRD) using a Rigaku-D diffractometer with Cu K_α radiation. The morphology was investigated by a scanning electron microscope (SEM), equipped with an energy dispersive X-ray spectrometer (EDS) suitable for element identification. Transmission electron microscopy (TEM) observation and scanning TEM (STEM)-EDS elemental mapping were performed by a FEI Tecnai G^2 F20. UV-diffuse reflection spectra were recorded by a Perkin Elmer Lambda 900 spectrophotometer. The photoluminescence (PL) spectra of the photocatalysts were obtained by a Hitachi F-4500 spectrophotofluorometer with an excitation wavelength of 325 nm.

2.3 Photocatalytic testing

RhB was used as model dye to evaluate the photocatalytic activity of ZnO, $ZnWO_4$ and $ZnO–ZnWO_4$ samples. Photodegradation of RhB was carried out in a 250 mL Pyrex reactor filled with deionized water (60 mL) containing RhB (10 mg L^{-1}) and the photocatalysts (50 mg). The suspension was stirred for 30 min in the dark to obtain adsorption–desorption equilibrium of the dye before illumination. After irradiation with a 250 W Hg lamp ($\lambda = 365$ nm), a 5 mL aliquot was took out at different time intervals and immediately centrifuged. The RhB concentration in the clear solution was analysed by optical characteristic absorption at a wavelength of 553 nm for an RhB solution.

3 Results and discussion

Fig. 1 shows the XRD patterns of ZnO, $ZnWO_4$, and $ZnO–ZnWO_4$ composites calcined at 850 °C for 2 h. The standard XRD patterns of ZnO (Fig. 1a) and $ZnWO_4$ (Fig. 1b) are corresponding to the hexagonal wurtzite and monoclinic phases, respectively. The diffraction peaks of ZnO and $ZnWO_4$ samples match well with the standard XRD patterns. A peak related to ZnO was detected at $2\theta = 34.42°$ in Fig. 1b. No other impurity peaks were found in the XRD patterns. Fig. 1c displays the XRD patterns of the serials $ZnO–ZnWO_4$ composites. The intensity of the distinct peak indicates the different percentage content of individual ZnO and $ZnWO_4$, respectively. With increasing $ZnWO_4$ content, the crystallite sizes of ZnO calculated by the Scherre's equation were 43.97 nm, 39.55 nm, 37.74 nm and 37.40 nm, respectively. It indicates that the crystal growth of ZnO is inhibited by $ZnWO_4$.

Fig. 2 shows the representative XRD patterns of $Z-ZW_{0.08}$ samples calcined for 2 h at 750 °C, 850 °C and 950 °C, respectively. With increasing temperature, the Full Width at Half Maximum (FWHM) of diffraction peaks (101) for ZnO and (111) for $ZnWO_4$ are 0.249°, 0.219° and 0.189°, and 0.250°, 0.204° and
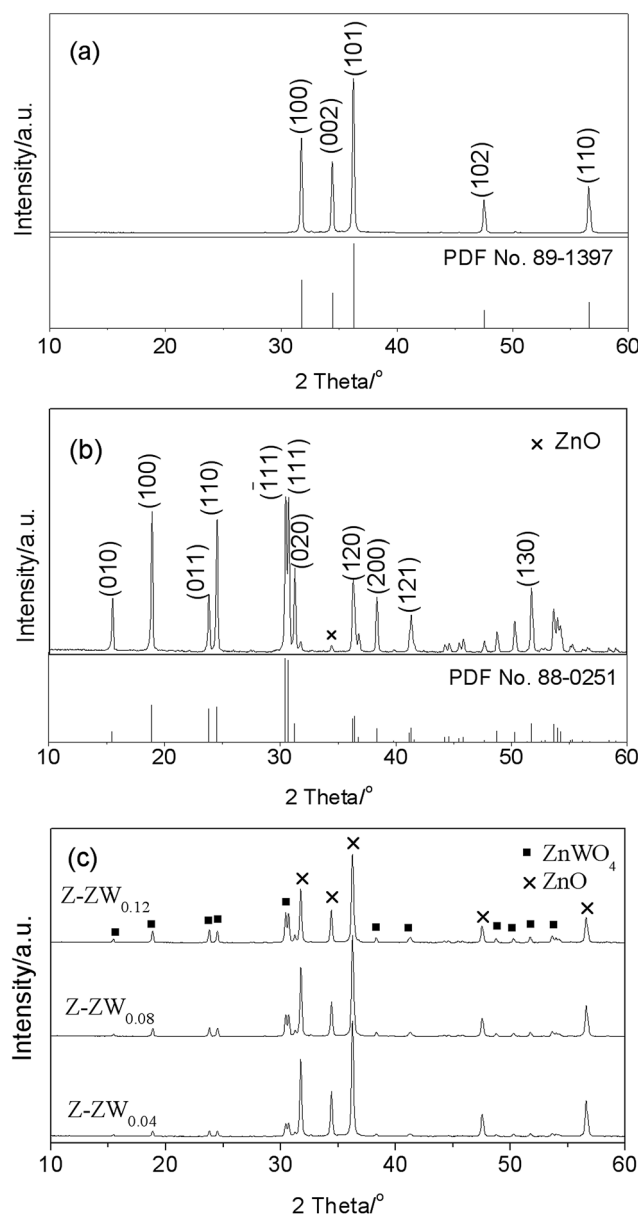

Fig. 1 XRD patterns of ZnO (a), $ZnWO_4$ (b), and $ZnO–ZnWO_4$ (c) composites calcined at 850 °C for 2 h.

0.198°, respectively, showing the peaks of both phases become sharper. It indicates that the crystallinity can be improved by raising calcining temperature, which is consistent with the published works.[3a]

The morphologies of the samples were observed by SEM. Fig. 3 shows the SEM images of ZnO, $ZnWO_4$, and $ZnO–ZnWO_4$ heterojunctions calcined at 850 °C for 2 h. It displays the rod-like ZnO with average length 3 μm and the needle-like ZnO with average length 4.5 μm. After loading $ZnWO_4$, the pearl necklace-like particles were found. Furthermore, hollow structures were observed at one side of the rod-like/needle-like particles as highlight by circles (Fig. 3b and c). With the increase of the $ZnWO_4$ content, the pearl necklace-like morphology become predominant and the hollow structure
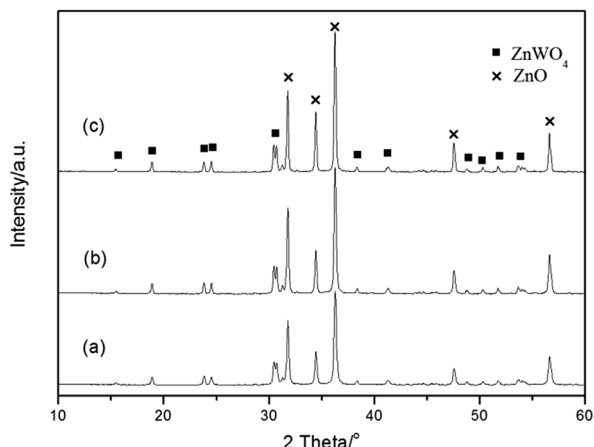
Fig. 2 XRD patterns of Z-ZW$_{0.08}$ calcined for 2 h at different temperatures, 750 °C (a), 850 °C (b), and 950 °C (c).

diminished gradually, as shown in Fig. 3d. The particle size of ZnO decreased with increasing ZnWO$_4$ content. ZnO with smaller particle size and crystallite size contributes to their influence on charge carrier recombination rate and specific surface area, which may enhance the photocatalytic performance.[15] For the ZnWO$_4$ (Fig. 3e), some particles adhere to slantprism-like ZnWO$_4$ surface, while others agglomerated. Clearly, the morphologies of ZnO–ZnWO$_4$ samples depend on the molar ratio of ZnO to ZnWO$_4$.

The element composition of the ZnWO$_4$ sample was analyzed by EDS. Zn and W elements were detected in

slantprism-like shape ZnWO$_4$ sample and the element ratio of W to Zn was *ca.* 1 : 1 (Fig. 3f, carbon derived from the conductive adhesive). However, only Zn and O elements were detected in agglomerated ZnWO$_4$ particles (Fig. 3g). EDS confirmed that there is a small amount of ZnO in the ZnWO$_4$ sample, which is consistent with the XRD result.

As one kind of ZnO–ZnWO$_4$ heterojunctions, Z-ZW$_{0.08}$ was further characterized by TEM and STEM-EDS elemental mapping. The low-magnification TEM image demonstrates that the Z-ZW$_{0.08}$ shows pearl necklace-like morphology, as presented in Fig. 4a. The high-resolution TEM (HR-TEM) image (Fig. 4b) clearly displays that the ZnWO$_4$ nanoparticles with a particle size of about 3 nm distribute on the surface of ZnO. The elemental mapping (Fig. 4c) shows that W element is uniform distributed in the sample, which demonstrates ZnWO$_4$ nanoparticles distribute well on the surface of ZnO.

The ultraviolet-visible (UV-vis) absorption spectra of ZnO, ZnWO$_4$ and ZnO–ZnWO$_4$ composites are shown in Fig. 5. The band gap values (E_g) of the photocatalysts were determined by extrapolating the linear part of the plots of $(\alpha h\nu)^2$ *versus* the energy of exciting light.[9b] The calculated band gap energies of ZnO, Z-ZW$_{0.08}$, Z-ZW$_{0.12}$, and ZnWO$_4$ are 3.20 eV, 3.19 eV, 3.18 eV and 3.17 eV, respectively. It can be seen that the presence of ZnWO$_4$ caused the absorption shift towards long wavelength region, which may result from the formation of the energy level of vacancy oxygen since W^{6+} was doped into the crystal lattice of ZnO.[16]

The photocatalytic activities of the powders were tested by degradation of RhB solution under UV light irradiation. Fig. 6 shows the effect of calcination temperature on the photocatalytic activity of Z-ZW$_{0.08}$ sample. The highest efficiency was obtained when the sample was calcined at 850 °C, whereas the powders calcined at 750 °C and 950 °C are less active. The
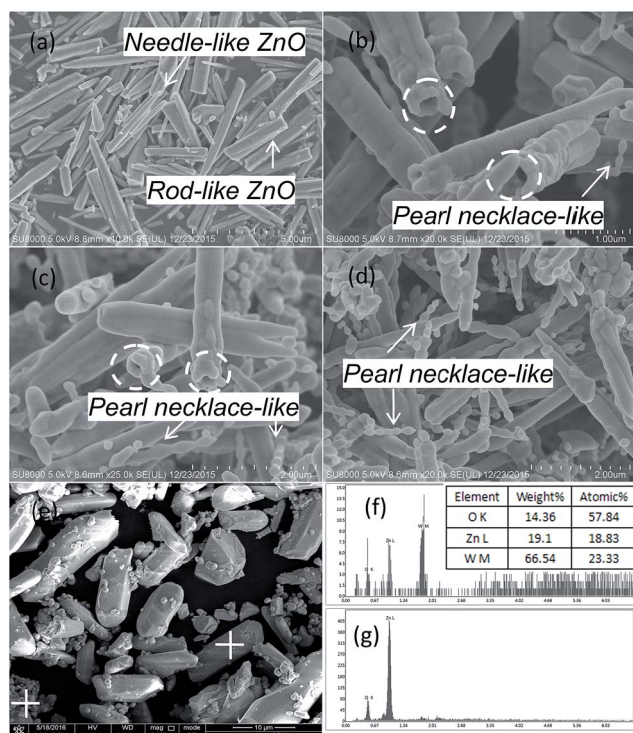

Fig. 3 SEM micrographs of ZnO (a), Z-ZW$_{0.04}$ (b), Z-ZW$_{0.08}$ (c), Z-ZW$_{0.12}$ (d), ZnWO$_4$ (e), and EDS spectra of ZnWO$_4$ (f and g).
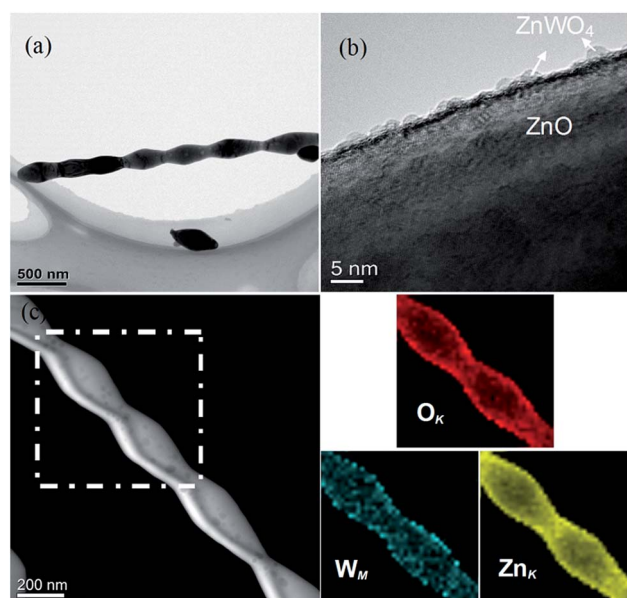

Fig. 4 Low-magnification TEM (a), HR-TEM (b) images and STEM-EDS elemental mapping (c) of Z-ZW$_{0.08}$.
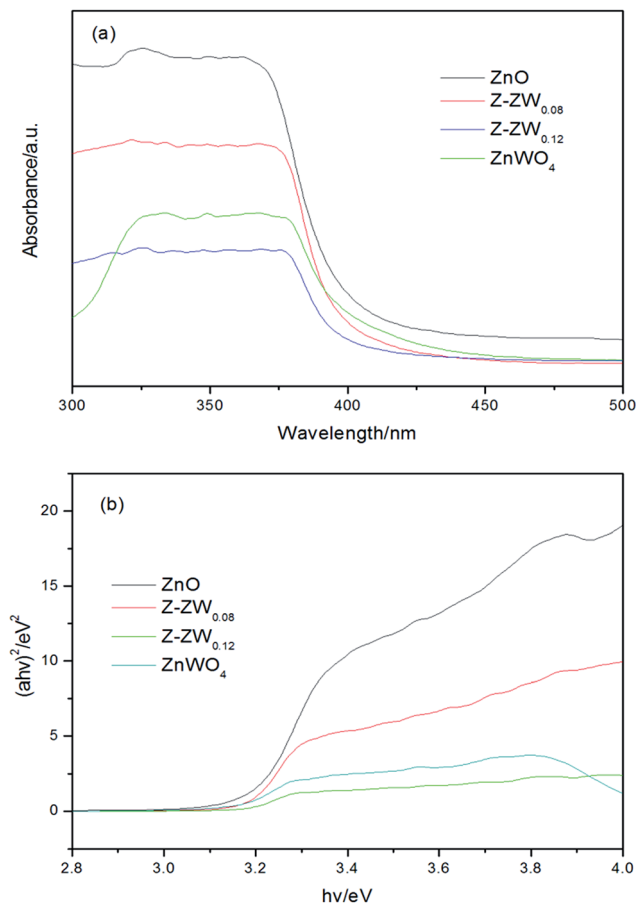
Fig. 5 (a) UV-vis diffuse reflectance spectra, (b) $(\alpha h\nu)^2$ versus energy plots.
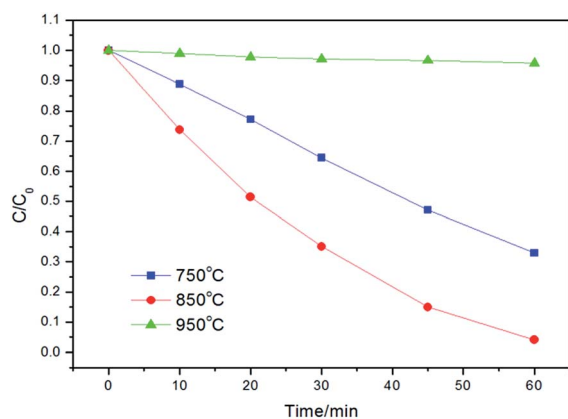

Fig. 6 Photodegradation kinetics of RhB over Z-ZW$_{0.08}$ calcined for 2 h at different temperatures.

crystallinity of the sample increased with raising the calcination temperature, which reduced the recombination of photo-generated carriers.[9b,17] However, the higher calcination temperature resulted in the decrease of surface area, larger particle size, and decrease of dispersion in solution, which caused an adverse effect on the harvest of light and the adsorption of dye, producing a negative effect on activity.

Fig. 7a and b show the kinetics of RhB degradation in the presence of ZnO, ZnWO$_4$ and ZnO–ZnWO$_4$ composites calcined at 850 °C. The degradation of RhB could be described by the first-order kinetics of $-\ln(C_t/C_0) = kt$, where k is the apparent reaction rate constant, and C_0 and C_t are the initial concentration and the concentration at reaction time of RhB, respectively. After 60 min of UV irradiation, 8%, 71%, 91%, 96% and 86% of RhB were degraded by ZnWO$_4$, ZnO, Z-ZW$_{0.04}$, Z-ZW$_{0.08}$ and Z-ZW$_{0.12}$, respectively. The photoactivity of ZnWO$_4$ was very low compared to that of ZnO, but all the ZnO–ZnWO$_4$ samples showed higher photocatalytic activity than single ZnO or ZnWO$_4$. The photocatalytic activities of the composites were found to be related to the ZnO/ZnWO$_4$ molar ratio. The Z-ZW$_{0.08}$ shows the highest photocatalytic activity. In the Z-ZW$_{0.12}$ sample, a large amount of free ZnWO$_4$ particles exists, which are less activity, leading to a lower photoactivity.[4] Therefore, there is an optimum ZnWO$_4$ content that leads to maximum photocatalytic efficiency. The k values were calculated by the initial slope of the concentration versus time profiles (Fig. 7b). It can be seen that Z-ZW$_{0.08}$ sample owns the highest rate constant of 0.035 min^{-1}.

The recombination of electron–hole pairs can release energy, which can be detected by PL emission. Lower photo-luminescence intensity indicates a lower recombination of electron–hole pairs, resulting in superior photocatalytic activity.[1e] The PL spectra of the ZnO, ZnWO$_4$ and Z-ZW$_{0.08}$ samples obtained at the excitation wavelength of 325 nm are shown in Fig. 7c. The PL intensities of ZnO and Z-ZW$_{0.08}$ could be ignored compared with that of ZnWO$_4$. The enlarged PL spectra of ZnO and Z-ZW$_{0.08}$ at the range of 400–600 nm in the inset panel shows that the composites sample has a lower recombination rate of photogenerated electron–hole pairs. The PL results display the importance of the heterostructure of ZnO/ZnWO$_4$ in blocking the recombination of electrons and holes. In order to
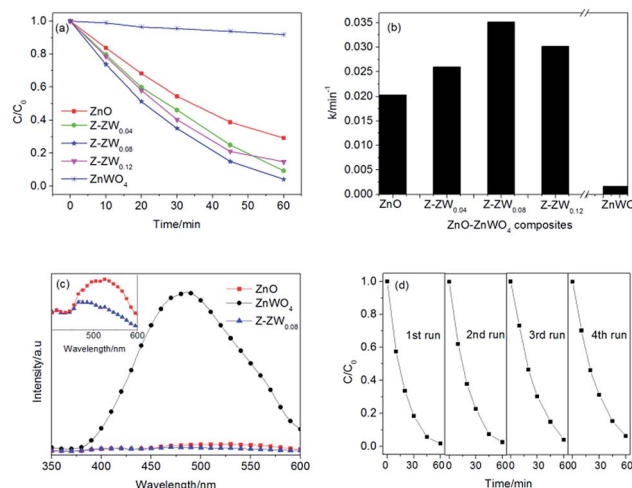

Fig. 7 Photodegradation kinetics of RhB over ZnO, ZnWO$_4$, and ZnO–ZnWO$_4$ composites calcined at 850 °C for 2 h (a and b); room temperature PL spectra of as-synthesized samples obtained at the excitation wavelength of 325 nm (c); cycling runs for the photocatalytic degradation of RhB over Z-ZW$_{0.08}$ (d).

evaluate the stability of the Z-ZW$_{0.08}$ photocatalyst, a recycling test was carried out. The result is displayed in Fig. 7d. The degradation rate of RhB still remained over 90% after four cycles.

The enhancement in the photocatalytic activity of Z-ZW$_{0.08}$ sample arose from the heterojunctions between ZnO and ZnWO$_4$. The formation of the heterojunctions may improve the charge separation efficiency of photoexcited carriers in ZnO–ZnWO$_4$ composites. The potentials of valence band (VB) and conduction band (CB) of a semiconductor can be calculated according to the following empirical equations:

$$E_{VB} = X - E^e + 0.5E_g \qquad (1)$$

$$E_{CB} = E_{VB} - E_g \qquad (2)$$

where E_{VB} is the valence band edge potential, E_{CB} is the conduction band edge potential, X is the electronegativity of the semiconductor, which is the geometric mean of the electronegativity of the constituent atoms, E^e is the energy of free electrons on the hydrogen scale (about 4.5 eV), E_g is the band gap energy of the semiconductor.[1e,1h] Based on the eqn (1) and (2), the E_{CB} potentials of ZnO and ZnWO$_4$ were calculated to be −0.31 and 0.145 eV, respectively. The E_{VB} potentials of ZnO and ZnWO$_4$ are determined to be 2.89 and 3.315 eV, respectively. A mechanism for electron–hole separation and transport of ZnO–ZnWO$_4$ heterojunctions is proposed (Fig. 8).

Both ZnO and ZnWO$_4$ are n-type semiconductors and their band gaps match well with each other to form type II heterojunction.[18] The CB of ZnO is lower than that of ZnWO$_4$, thus photogenerated electrons transfer easily from CB of ZnO to that of ZnWO$_4$ through the well-developed interface, and the photoinduced holes shift from VB of ZnWO$_4$ to that of ZnO. Therefore, the ZnO–ZnWO$_4$ heterojunctions could act as an active center for hindering the rapid recombination of photogenerated electron–hole pairs. The electrons accumulated in the CB of ZnWO$_4$ can be captured by O$_2$ to produce superoxide radical ($\cdot$O$_2^-$) and hydrogen peroxide (H$_2$O$_2$), which can interact to produce a powerful oxidant (hydroxyl radical, $\cdot$OH) to decompose RhB. The holes accumulated in the VB of ZnO take

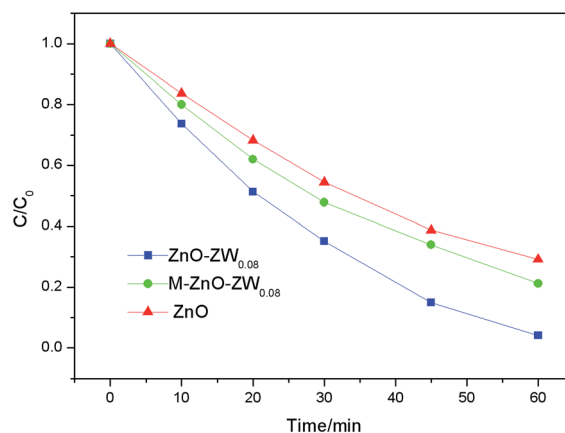Fig. 9 Photocatalytic degradation of RhB over ZnO, Z-ZW$_{0.08}$, and M-Z-ZW$_{0.08}$.

part in the oxidation process to make OH$^-$ or H$_2$O species to produce reactive hydroxyl radicals.[1a,19]

To further confirm the heterojunctions effect, the photodegradation of RhB was also studied in the presence of a mechanical mixture of ZnO and ZnWO$_4$, which is labelled as M-Z-ZW$_{0.08}$. As shown in Fig. 9, the photocatalytic activity of the M-Z-ZW$_{0.08}$ sample is higher compared to that of ZnO but much lower than that of Z-ZW$_{0.08}$. This result demonstrates that the Z-ZW$_{0.08}$ composite can form intimate interface in the heterojunctions, rather than form loose interfaces existing in the mechanically mixed samples.

4 Conclusions

The pearl necklace-like ZnO–ZnWO$_4$ heterojunctions were successfully synthesized by precipitation method followed by calcination. The photocatalytic activity of ZnO–ZnWO$_4$ composites was found to be dependent on the calcination temperature and ZnO/ZnWO$_4$ mol ratio. The photoefficiency of the ZnO–ZnWO$_4$ heterojunctions was better than that of ZnO and ZnWO$_4$. Z-ZW$_{0.08}$ composite powders show the best photocatalytic degradation performance for degradation of RhB with degradation efficiency about 96% under UV irradiation in 60 min. The enhanced photoactivity is due to the reduction in the recombination of photo-generated electrons and holes. This work provides a facile method to design and fabricate ZnO–ZnWO$_4$ heterojunctions with special morphology.
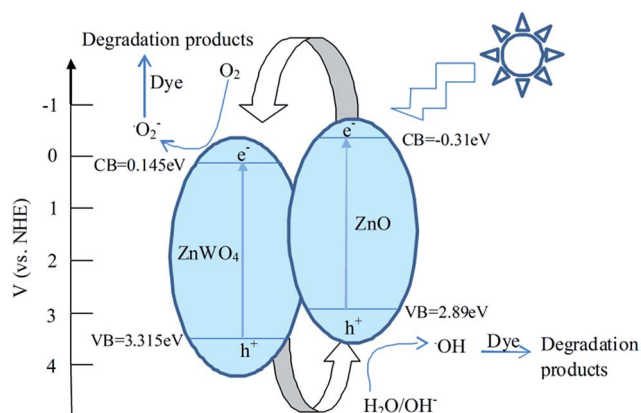
Acknowledgements

Fig. 8 Degradation schematic mechanism of RhB over ZnO–ZnWO$_4$ composites.

Notes and references

1 (a) W. Li, L. Y. Cao, X. G. Kong, J. F. Huang, C. Y. Yao, J. Fei and J. Y. Li, *RSC Adv.*, 2016, **6**, 23783; (b) S. Adhikari, D. Sarkar and G. Madras, *RSC Adv.*, 2015, **5**, 11895; (c) D. Li, R. Shi, C. S. Pan, Y. F. Zhu and H. J. Zhao, *CrystEngComm*, 2011, **13**, 4695; (d) M. Sharma, D. Das, A. Baruah, A. Jain and A. Ganguli, *Langmuir*, 2014, **30**, 3199; (e) X. Lin, B. Wei, X. X. Zhang, M. S. Song, S. Y. Yu, Z. Y. Gao, H. J. Zhai, L. N. Zhao and G. B. Che, *Sep. Purif. Technol.*, 2016, **169**, 9; (f) X. Lin, D. Xu, Y. Xi, R. Zhao, L. N. Zhao, M. S. Song, H. J. Zhai, G. B. Che and L. M. Chang, *Colloids Surf., A*, 2017, **513**, 117; (g) X. Lin, D. Xu, J. Zheng, M. S. Song, G. B. Che, Y. S. Wang, Y. Yang, C. Liu, L. N. Zhao and L. M. Chang, *J. Alloys Compd.*, 2016, **688**, 891; (h) X. Lin, D. Xu, S. S. Jiang, F. Xie, M. S. Song, H. J. Zhai, L. N. Zhao, G. B. Che and L. M. Chang, *Catal. Commun.*, 2017, **89**, 96.

2 (a) C. Q. Zhu, B. G. Lu, Q. Su, E. Q. Xie and W. Lan, *Nanoscale*, 2012, **4**, 3060; (b) J. Zhai, X. Tao, Y. Pu, X. F. Zeng and J. F. Chen, *Appl. Surf. Sci.*, 2010, **257**, 393.

3 (a) Y. Hong, C. G. Tian, B. J. Jiang, A. P. Wu, Q. Zhang, G. H. Tian and H. G. Fu, *J. Mater. Chem. A*, 2013, **1**, 5700; (b) X. Y. Zhang, J. Q. Qin, Y. N. Xue, P. F. Yu, B. Zhang, L. M. Wang and R. P. Liu, *Sci. Rep.*, 2014, **4**, 4596; (c) T. Sahoo, M. Kim, J. Baek, S. Jeon, J. Kim, Y. Yu, C. Lee and I. Lee, *Mater. Res. Bull.*, 2011, **46**, 525; (d) K. Sinha, M. Basu, M. Pradhan, S. Sarkar and T. Pal, *Chem.–Eur. J.*, 2010, **16**, 7865; (e) J. Xie, H. Wang, M. Duan and L. H. Zhang, *Appl. Surf. Sci.*, 2011, **257**, 6358.

4 X. W. Jiang, X. R. Zhao, L. B. Duan, H. Shen, H. N. Liu, T. Hou and F. G. Wang, *Ceram. Int.*, 2016, **42**, 15160.

5 B. X. Li and Y. F. Wang, *J. Phys. Chem. Solids*, 2011, **72**, 1165.

6 (a) S. F. Chen, W. Zhao, W. Liu and S. J. Zhang, *Appl. Surf. Sci.*, 2008, **255**, 2478; (b) L. Wu, J. Xing, Y. Hou, F. Y. Xiao, Z. Li and H. G. Yang, *Chem.–Eur. J.*, 2013, **19**, 8393.

7 S. Balachandran, N. Prakash, K. Thirumalai, M. Muruganandham, M. Sillanpää and M. Swaminathan, *Ind. Eng. Chem. Res.*, 2014, **53**, 8346.

8 A. Hamrouni, N. Moussa, F. Parrino, A. Di Paola, A. Houas and L. Palmisano, *J. Mol. Catal. A: Chem.*, 2014, **390**, 133.

9 (a) I. Validzic, T. Savic, R. Krsmanovic, D. Jovanovic, M. Novakovic, M. Popovic and M. Comor, *Mater. Sci. Eng., B*, 2012, **177**, 645; (b) A. Hamrouni, N. Moussa, A. Di Paola, F. Parrino, A. Houas and L. Palmisano, *Appl. Catal., B*, 2014, **154–155**, 379; (c) F. Z. Wang, W. J. Li, S. N. Gu, H. D. Li, X. T. Liu and M. Z. Wang, *ACS Sus. Chem. Eng.*, 2016, **4**, 6288.

10 Y. Wang, Q. S. Wang, X. Y. Zhan, F. M. Wang, M. Safdar and J. He, *Nanoscale*, 2013, **5**, 8326.

11 Z. Amouzegar, R. Naghizadeh, H. R. Rezaie, M. Ghahari and M. Aminzare, *Ceram. Int.*, 2015, **41**, 1743.

12 M. Mancheva, R. Iordanova and Y. Dimitriev, *J. Alloys Compd.*, 2011, **509**, 15.

13 G. L. Huang, S. C. Zhang, T. G. Xu and Y. F. Zhu, *Environ. Sci. Technol.*, 2008, **42**, 8516.

14 T. Montim, V. Gombac, A. Hameed, L. Felisan, G. Adami and P. Fornasiero, *Chem. Phys. Lett.*, 2010, **498**, 113.

15 J. Becker, K. R. Raghupathi, J. S. Pierre, D. Zhao and R. T. Koodali, *J. Phys. Chem. C*, 2011, **115**, 13844.

16 C. L. Yu, K. Yang, Q. Shu, J. C. Yu, F. F. Cao and X. Li, *Chin. J. Catal.*, 2011, **32**, 555.

17 B. Ohtani, Y. Ogawa and S. Nishimoto, *J. Phys. Chem. B*, 1997, **101**, 3746.

18 R. Marschall, *Adv. Funct. Mater.*, 2014, **24**, 2421.

19 (a) A. Di Paola, M. Bellardita, R. Ceccato, L. Palmisano and F. Parrino, *J. Phys. Chem. C*, 2009, **113**, 15166; (b) S. Kundu, *J. Mater. Chem. C*, 2013, **1**, 831.